

# Long-term variations of turbulent transport coefficients in a solarlike convective dynamo simulation

F. A. Gent<sup>1,\*</sup> | M. J. Käpylä<sup>1,2</sup> | J. Warnecke<sup>2</sup>

<sup>1</sup>Department of Computer Science, ReSoLVE Centre of Excellence, Aalto University, Helsinki, Finland

<sup>2</sup>Max Planck Institute for Solar System Research, Göttingen, Germany

\*Correspondence

F. A. Gent, Department of Computer Science, ReSoLVE Centre of Excellence, Aalto University, PO Box 15400, Helsinki 00760, Finland.  
Email: [frederick.gent@aalto.fi](mailto:frederick.gent@aalto.fi)

Funding Information

Academy of Finland ReSoLVE Centre of Excellence, 272157. European Union's Seventh Framework Programme, FP7/2007-2013. REA, 623609. Finnish Ministry of Education.

The Sun, aside from its 11-year sunspot cycle, is additionally subject to long-term variation in its activity. In this work, we analyze a solarlike convective dynamo simulation, containing approximately 60 magnetic cycles, exhibiting equatorward propagation of the magnetic field, multiple frequencies, and irregular variability, including a missed cycle and complex parity transitions between dipolar and quadrupolar modes. We compute the turbulent transport coefficients, describing the effects of the turbulent velocity field on the mean magnetic field, using the test-field method. The test-field analysis provides a plausible explanation of the missing cycle in terms of the reduction of  $\alpha_{\phi\phi}$  *in advance of* the reduced surface activity and enhanced downward turbulent pumping *during* the event to confine some of the magnetic field at the bottom of the convection zone, where the local maximum of magnetic energy is observed during the event. At the same time, however, a quenching of the turbulent magnetic diffusivities is observed, albeit differently distributed in depth compared to the other transport coefficients. Therefore, dedicated mean-field modeling is required for verification.

KEYWORDS

stars: magnetic fields – magnetohydrodynamics (MHD) – convection – turbulence – methods: numerical

## 1 | INTRODUCTION

Simulations of stellar global convection with spontaneous dynamo action have become abundant during the recent years, thanks to the ever-increasing computational resources. In recent years, we have witnessed the emergence of realistic solarlike dynamo solutions, where the large-scale magnetic field shows polarity reversals and equatorward propagation (e.g., Augustson et al. 2015; Ghizaru et al. 2010; Käpylä et al. 2012) with the important realization that the presence of a shear layer at the bottom of the convection zone (CZ) is not important in obtaining such solutions. In addition to the basic solar cycle, some models also capture multiple dynamo modes in one and the same simulation (Beaudoin et al. 2016; Käpylä et al. 2016) and also exhibit irregular behavior resembling, at least to some extent, grand minima (Augustson et al. 2015; Käpylä et al. 2016, 2017).

It turns out that the equatorward migration direction of the large-scale magnetic field in these simulations can be well

explained with the propagation direction of an  $\alpha\Omega$  dynamo wave following the Parker–Yoshimura sign rule (Parker 1955; Yoshimura 1975) as shown in several studies (Guerrero et al. 2016; Käpylä et al. 2016, 2017; Warnecke et al. 2014, 2016) using the kinetic and magnetic helicities as proxies to compute the  $\alpha$ -effect. However, this result crucially relies on the sign and distribution of the  $\alpha$ -effect, and therefore, a measurement of it rather than estimations using proxies would be desirable (Warnecke et al. 2017).

It must be regarded as a major breakthrough that solarlike dynamo solutions can now be obtained from global convection simulations. This in itself, however, does not as yet reveal the internal workings of the solar dynamo. The next challenge is to carefully analyze such simulation results to pinpoint how various possible mechanisms, namely differential rotation, meridional circulation, and turbulent effects, affect the evolution of the mean magnetic field. This is another nontrivial task, especially where the measurement of the turbulent effects is concerned.

One method to determine the turbulent transport coefficients, and therefore the effect of turbulent flow on the evolution of the mean magnetic field, is the test-field method (Schrinner et al. 2005, 2007). This method makes use of the mean-field approximation and utilizes linearly independent test fields, which do not backreact on the dynamo solution, but are merely used to measure the turbulent transport coefficients. We assume that the large-scale field is axisymmetric about the polar axis and can therefore be described by a mean field averaged over the azimuthal direction satisfying the Reynolds averaging rules, required for the mean-field approximation to hold.

This method has successfully been applied to simulations of planetary interiors (e.g., Schrinner et al. 2005, 2007, 2012) and various other setups (see, e.g., Brandenburg et al. 2010 and references therein). Recently, it was applied, for the first time, to solarlike convective dynamo solutions by Warnecke et al. (2017). The general conclusion is that turbulent effects play an important role in the dynamics and evolution of the mean magnetic field in these simulations. More specifically, the authors found that the components of  $\alpha$ -tensor, and therefore the  $\alpha$ -effect, are not well described by the isotropic Second Order Correlation Approximation (SOCA) expression based on kinetic helicity. Furthermore, the turbulent pumping significantly alters the effective meridional circulation acting on the magnetic field. Global convection simulations have previously challenged the flux transport dynamo paradigm, as multiple circulation cells are more a rule than an exception (see, e.g., Käpylä et al. 2014), while the one-cell circulation important for these dynamo models seems unlikely. The new results, in practice, imply that even though the meridional flow measurement accuracy improved to provide a reliable determination of the pattern, the turbulent effects would still elude observations, making the measurement of the effective meridional circulation pattern relevant for the mean magnetic field impossible. Moreover, all the turbulent transport coefficients show variation along the magnetic cycle, and additionally strong random variation, the former of which can play an important role in the saturation process of the dynamo. Warnecke et al. (2017) additionally found that coefficients calculated with methods based on linear regression as used in Racine et al. (2011) and Augustson et al. (2015) can be incorrect and therefore lead to misleading conclusions for the dynamo mechanism, that is, the wrong propagation direction of the dynamo wave.

The solarlike dynamo solutions have been integrated over timescales of the order of a hundred magnetic cycles and have revealed interesting long-term phenomena (a longer cycle, reminiscent of the Gleissberg cycle, and irregular behavior, including the disappearance of surface magnetic fields), as reported in Käpylä et al. (2016). Simulations evolving an equivalent time span, but over fewer magnetic cycles, and without significant irregularity, have also been produced by Passos & Charbonneau (2014) and Norton et al. (2014). In the study of Käpylä et al. (2016), no evident reason due

to differential rotation nor meridional circulation could be found for the irregular behavior, while the turbulent transport coefficients were not determined. All the interesting behavior was, however, in one way or another related to the properties of and competition between the different dynamo modes present in the system.

Therefore, it is of great interest to understand why and when different types of dynamo modes become excited in such a system. For this purpose, the turbulent transport coefficients need to be determined, which is the goal of this paper. We study a dynamo solution that was restarted from a snapshot of the Käpylä et al.'s (2016) simulation, but varying slightly the boundary conditions and including the test-field module, somewhat altering the length of time step. Consequently, we obtain a statistically equivalent dynamo solution, such that it differs only locally in time. We concentrate our analysis on understanding the epochs of varying parity of the basic magnetic cycle and one irregular epoch when the surface magnetic field vanished from the northern hemisphere for a timescale of the order of one cycle.

## 2 | MODEL AND SETUP

The simulation setup is the same as in Käpylä et al. (2016), and a detailed description of the general model can be found in Käpylä et al. (2013) and will not be repeated here. We model the solar CZ as a spherical wedge in spherical polar coordinates:  $0.7 R \leq r \leq 1 R$  in radius,  $15^\circ \leq \theta \leq 165^\circ$  in latitude, and  $0^\circ \leq \phi \leq 90^\circ$  in azimuth, where  $R$  is the solar radius. We solve the compressible magnetohydrodynamic (MHD) equations for the plasma density  $\rho$ , velocity  $u$ , specific entropy  $s$ , and the magnetic vector potential  $A$ , with  $B = \nabla \times A$ , assuming an ideal gas for the equation of state. We include the effects of gravity and rotation on the fluid evolution. The details of the setup, the exact form of the equations, and the initial conditions can be found in Käpylä et al. (2013, 2016) and Warnecke et al. (2014).

The spherical wedge is assumed to be periodic along the azimuthal direction. The boundary conditions at the inner radial and both latitudinal boundaries satisfy a perfect conductor and a radial magnetic field condition at the outer radial boundary. The present setup includes a small correction to the radial perfect conductor condition in comparison with Käpylä et al. (2016). This adds an extra term that must be included when using spherical rather than Cartesian coordinates to fulfill vanishing tangential currents. However, the inclusion of this term does not affect the overall statistics of the dynamo solution. The flow obeys a stress-free condition at all radial and latitudinal boundaries. For entropy, the lower radial boundary condition is described by a constant heat flux into the wedge, and at the upper boundary, the temperature obeys a blackbody condition. The thermodynamic quantities have zero derivatives leading to vanishing energy fluxes at the latitudinal boundaries.

Our model can be characterized with fluid and magnetic Prandtl numbers

$$\text{Pr}_{\text{SGS}} = \frac{\nu}{\chi_{\text{SGS}}^m} = 1, \quad \text{Pr}_M = \frac{\nu}{\eta} = 1,$$

Reynolds numbers

$$\text{Re} = \frac{u_{\text{rms}}}{\nu k_f} = 29, \quad \text{Re}_M = \frac{u_{\text{rms}}}{\eta k_f} = 29,$$

and Coriolis number

$$\text{Co} = 2 \frac{\Omega_0}{u_{\text{rms}} k_f} = 9.5,$$

where  $\nu$  is the kinematic viscosity,  $\chi_{\text{SGS}}^m$  is the turbulent heat diffusion at the middle of the CZ,  $\eta$  is the magnetic diffusivity, and  $\Omega_0$  is the rotation rate. Here, the wave number of the largest vertical scale in the CZ is  $k_f = 2\pi/0.3R \approx 21/R$  and

$$u_{\text{rms}} = \sqrt{\frac{3}{2} \langle u_r^2 + u_\theta^2 \rangle_{r\theta\phi}}$$

is the rms velocity without the  $\phi$  component, as  $u_\phi$  is dominated by the differential rotation. The value of the magnetic Reynolds number corresponds to around three times the critical value for the dynamo to be excited. We also define the meridional distribution of the turbulent velocity:

$$u'_{\text{rms}}(r, \theta) = \langle \overline{u'^2} \rangle_t^{1/2},$$

where we use the mean-field decomposition into mean flow  $\bar{U}$  and fluctuating flow  $u' = u - \bar{U}$ . The mean is calculated using the azimuthal average. We apply a similar decomposition for the magnetic field:  $B = \bar{B} + b'$ . In this paper, we additionally use a decomposition into time average  $\langle f \rangle_t$  and variation  $f^\text{v}$  for such a quantity  $f$ . The turbulent transport coefficients presented are typically normalized by either

$$\alpha_0 = \frac{1}{3} u'_{\text{rms}} \quad \text{or} \quad \eta_{t0} = \frac{1}{3} \tau u'^2_{\text{rms}}$$

as appropriate. An estimate of the convective turnover time is  $\tau = H_p \alpha_{\text{MLT}} / u'_{\text{rms}}$ , where  $H_p = -(\partial \ln \bar{p} / \partial r)^{-1}$  is the pressure scale height and the mixing length parameter,  $\alpha_{\text{MLT}}$ , is here set to be 5/3.

To present our results in physical units, we invoke normalization based on the solar rotation rate  $\Omega_\odot = 2.7 \times 10^{-6} \text{ s}^{-1}$  and the density at the bottom of convection of the Sun. For a detailed description and discussion, relating the simulations to real stars, we refer to Käpylä et al. (2013, 2014, 2016) and Warnecke et al. (2014). The simulation is performed with the Pencil Code,<sup>1</sup> which uses a high-order finite difference method for solving the compressible equations of MHD.

## 2.1 | Test-field method

In the test-field method (Schrinner et al. 2005, 2007; Warnecke et al. 2017), it is assumed that the turbulent electromotive force,  $\varepsilon = \overline{u'} \times b'$ , describing the effect of turbulence on the mean magnetic field, can be expressed as an expansion

in terms of  $\bar{B}$ , where contributions from higher derivatives are neglected and scale separation is assumed. Following Krause & Rädler (1980), this leads to

$$\varepsilon = \alpha \cdot \bar{B} + \gamma \times \bar{B} - \beta \cdot (\nabla \times \bar{B}) - \delta \times (\nabla \times \bar{B}) - \kappa \cdot (\nabla \bar{B})^{(s)}. \quad (1)$$

Here,  $\alpha$  is giving rise to the  $\alpha$ -effect (Steenbeck et al. 1966).  $\gamma$  describes changes in the mean magnetic field due to an effective velocity (or “turbulent pumping,” e.g., Ossendrijver et al. 2002).  $\beta$  characterizes the turbulent diffusion.  $\delta$  enables what is known as the Rädler effect (Rädler 1969) and the shear current effect. The rank-three tensor,  $\kappa$ , with the symmetric part of the derivative tensor,  $(\nabla \bar{B})^{(s)}$ , does not yet have an established physical interpretation. To calculate the coefficients of Equation (1), we simultaneously solve for the evolution of fluctuating magnetic fields using nine independent, axisymmetric test fields and the flow field from the global simulation. From the nine test magnetic fields and their corresponding fluctuations, we are then able to calculate nine electromotive forces and invert for all coefficients in Equation (1). To avoid the eigensolution of the test-field problem becoming unstable, we reinitialize the test fields to zero at regular time intervals, which are typically much larger than the turnover time and much shorter than the magnetic cycle. For the analysis, we filter out transient time moments just before and after the resetting. The same technique was used in Warnecke et al. (2017). Further details and discussions about the theoretical background, the physical interpretation, and the shortcomings of the test-field method can be found in Schrinner et al. (2005, 2007) and Warnecke et al. (2017).

## 3 | RESULTS

### 3.1 | Dynamo characteristics

The simulation is continued from an original run of Käpylä et al. (2016) near year 25, the dynamo having reached a statistical steady state, and now with the addition of the test fields. A brief interval of transitional perturbation occurs due to the above-mentioned reformulation of the lower magnetic boundary condition, and this has been excluded from the analysis presented here.

To recap, the present simulation exhibits a solarlike differential rotation with the local minima at midlatitudes together with a multicellular meridional circulation. The main dynamo mode has a mean cycle period of around 5 years and shows a clear equatorward migration. It can be well described by a propagating dynamo wave based on the negative shear due to the local minima at midlatitudes and a positive  $\alpha$ -effect in this region (Käpylä et al. 2016).

With the inclusion of the test fields, the application of the Courant stability condition to the additional equations requires a slight reduction in the typical time step of about 20%. The system is highly chaotic, and the difference in time step produces a different realization of the turbulence, which diverges over time from the original simulation. The statistical

<sup>1</sup> <http://github.com/pencil-code/>

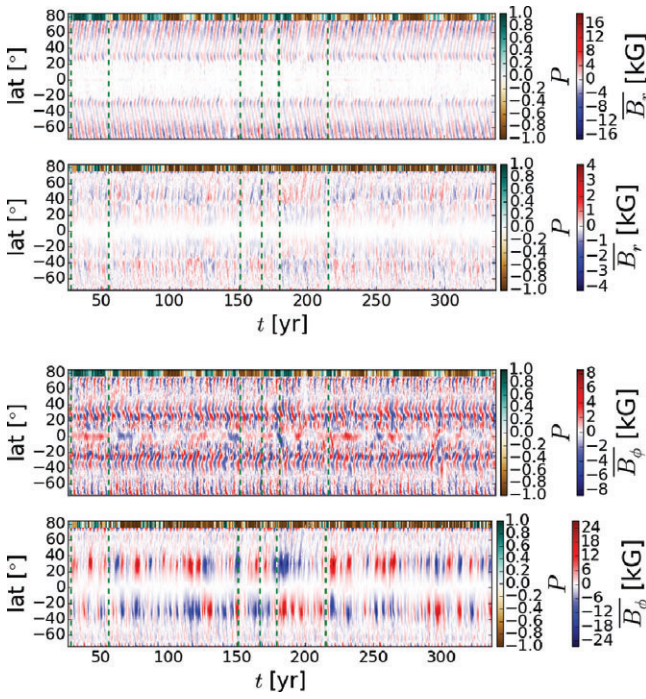


**FIGURE 1** Time–latitude plot of mean magnetic field components,  $\bar{B}_r$  (upper pair) and  $\bar{B}_\phi$  (lower pair). The first of each pair uses a radial slice near the surface ( $0.98R$ ) and the second from near the base of the convection zone (CZ) ( $0.72R$ ). The parity of the total magnetic field across the slice is depicted by the “barcode” along the top (brown–green). Vertical lines (green, dashed) indicate three epochs examined in detail.

properties of the system remain consistent, but the actual shifts in cycles, missing or weak cycles, now occur at different times. The current run, spanning over 300 years and amounting to roughly 60 magnetic cycles, has yet to exhibit a grand minimum. Such an event occurred in Käpylä et al. (2016) after about the 10 first magnetic cycles, but then took more than 80 magnetic cycles to reoccur. The current run, however, exhibits all the coexisting three cycles and long-term variation consistent with the original run. During 175–215 years, we also observe a short epoch over time when both the radial and azimuthal magnetic fields disappear from the northern hemisphere; we will later denote this time interval as the “missing cycle.” Although not clearly a grand minimum-type event, the turbulent transport coefficients exhibit interesting behavior during this interval, analyzed in detail in Section 3.2.3.

To illustrate some of these phenomena, Figure 1 includes two pairs of butterfly diagrams, that is, time–latitude diagrams, for mean magnetic field component  $\bar{B}_r$  (upper pair) and  $\bar{B}_\phi$  (lower pair) for the surface and the base of the CZ, respectively. The parity of the total field has been calculated for each slice as a function of time and is identified by the brown–green “barcode.” Parity is defined as follows:

$$P = \frac{E_{\text{even}} - E_{\text{odd}}}{E_{\text{even}} + E_{\text{odd}}}, \quad (2)$$

where  $E_{\text{even}}$  ( $E_{\text{odd}}$ ) is the magnetic energy (or other quantity) being equatorially symmetric (antisymmetric), that is, quadrupolar (dipolar) with extremum 1 ( $-1$ ).

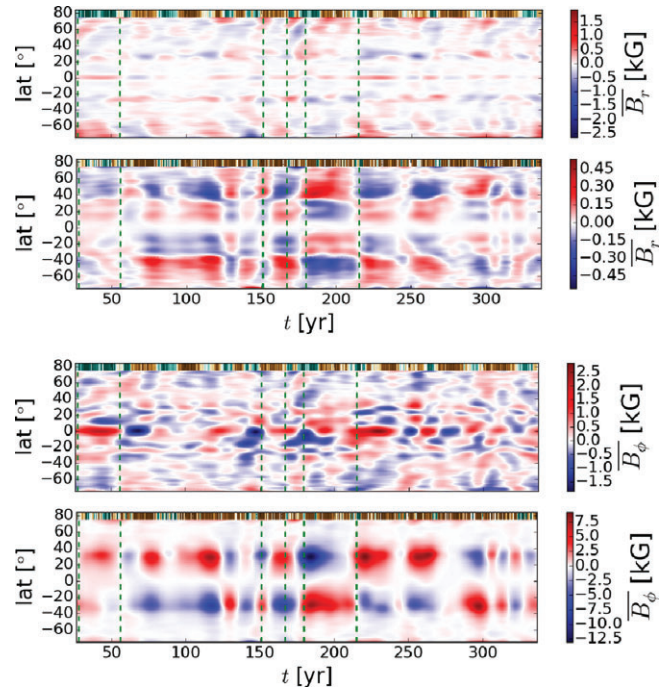


**FIGURE 2** Time–latitude plot of mean magnetic field components,  $\bar{B}_r$  (upper pair) and  $\bar{B}_\phi$  (lower pair) smoothed over approximately 50 years. Otherwise as Figure 1.

The characteristics of the field evolution are in excellent agreement with Käpylä et al. (2016, see their Figures 1 and 2). The field near the base is consistent between this model and theirs, indicating that differences in the implementation of the perfect conductor boundary condition have not qualitatively affected the solution. The length of the basic cycle is approximately 5 years and varies somewhat between the hemispheres (for detailed analysis, see Olspt et al. 2016). This is clearly evident in the surface magnetic field. In the base of the CZ, the basic cycle is still visible, but is clearly modulated by longer, rather irregular cycles. In the simulation run, with double the duration, analyzed in Olspt et al. (2016), two dominant cycles of roughly 50 and 100 years were found, and such cycles can also explain the variations seen in the current results. The basic cycle length fluctuates with distinct patterns in the north and south, to the extent that over a century, each hemisphere can produce a different number of cycles. In addition, both magnetic field components exhibit fluctuations in strength, most pronounced near the surface when the cycle in the northern hemisphere is very weak around 200 years, an epoch to which we refer to as the “missing cycle.” This is coincident with an interval of strong azimuthal field at the base (see Figure 2).

The parity, plotted as barcodes over the data in Figures 1 and 2, switches sign irregularly over time, and the parity profiles are quite distinct, perhaps independent, between the surface and the base. The base field parity is consistently more negative than that at the surface. The parity switches are not obviously associated with the basic cycle, and the long-term trends remain hidden in the raw data of Figure 1. To better

identify them, we apply temporal smoothing using a Gaussian kernel with a width of approximately 50 years.

The smoothed magnetic field components are displayed in Figure 2. The long-term cycle trends are now clearly visible, particularly for the magnetic field at the base. The smoothing helps to reveal the signatures of the long cycles also in the radial field near the surface, while the surface azimuthal field shows no evident modulation by the long cycles. The parity of the surface field shows some correlation with the long-term cycle seen in the bottom azimuthal field: The parity switches appear to occur often simultaneously with the changes in the polarity of the base mode.

In Figures 1 and 2, we also identify three epochs bounded by dashed green vertical lines, for further analysis. The first interval, 27–54 years, is identified with even parity in the surface magnetic field, and we shall refer to this as the “quadrupole epoch.” The second interval, 151–166 years, is identified with odd parity, which we shall refer to as the “dipole epoch.” These will be further examined in Section 3.2.2. The third interval, 175–215 years, is motivated by the decreased surface magnetic field strength seen and will be examined in Section 3.2.3.

### 3.2 | Turbulent transport coefficients

The derived turbulent transport coefficients are in excellent agreement with the results of Warnecke et al. (2017): near identical to their meridional profiles, averaged over the whole simulation time, and to their cyclic time variation over the basic cycle. In the current study, we concentrate on the long-term time evolution and zoom into epochs of interesting behavior.

#### 3.2.1 | Long-term variability

In order to see the five-year cycle more clearly, we zoom in at the first century of the simulation. In Figure 3, we display the butterfly diagrams for  $\bar{B}_r$  at the base of the CZ and the temporal variation in the turbulent tensor coefficients  $\alpha_{\phi\phi}^v$  and  $\beta_{\phi\phi}^v$ . The superscript  $v$  follows the notation convention of Warnecke et al. (2017), in which the temporal averages are subtracted, and then, the residual profile is suitably smoothed in time, in this case a temporal smoothing of 2.5 years, to retain the basic cycle. From these diagrams, it can be discerned that the cycle length of the transport coefficients is about half that of the magnetic field, due to the quadratic form of the Lorentz force mediating the effect of the mean field on the turbulent flow, agreeing with the results of Warnecke et al. (2017). More significantly, both the magnetic field and the turbulent coefficients exhibit strong fluctuations in the length and strength of their basic cycle, but also lower-frequency modes are visible. For example, a repeated long cycle in  $\bar{B}_r$  is visible at 75 and 115 years, with a matching equatorial quenching in  $\beta_{\phi\phi}^v$  at the same time and to a lesser extent in  $\alpha_{\phi\phi}^v$ .

To better expose these long-term trends, we apply a 50-year smoothing window to the full simulation and display the

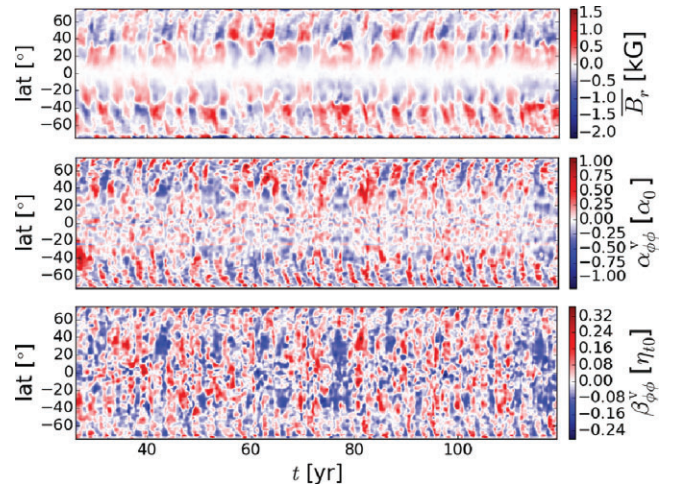


**FIGURE 3** Time–latitude plot near the base of the convection zone (CZ), depicting zoom-in of the early cycles in  $\bar{B}_r$ ,  $\alpha_{\phi\phi}^v$ , and  $\beta_{\phi\phi}^v$ . Temporal Gaussian smoothing has been applied with a width of approximately 2.5 years. We compute time averages of the transport coefficients over the whole time span of the simulation, subtract this profile to obtain the residuals, and use the sign of the average quantity to multiply the residual to indicate enhancement (diminution) with respect to the average profile.

diagonal components,  $\alpha_{ii}^v$ , paired from the surface and base of the CZ, as in Figure 4. Following Warnecke et al. (2017), we expect these components of  $\alpha$  to be the strongest and, therefore, most likely to influence the dynamo. At the surface, the cycles of the long-term variation in each  $\alpha$ -component have incoherent evolution across different latitudes, but the timescale of the variations appears quite similar for each tensor coefficient. The timescale also corresponds to the long-term variation typical of the surface magnetic field, as displayed in Figure 2, top and bottom panels.

The long-term cyclic variations at the base of the CZ are pronounced for  $\alpha_{rr}$  and  $\alpha_{\phi\phi}$ , being especially strong for the latter. These variations are not, however, coherent between each component of  $\alpha$ , although within each component the cycles are typically more common across all latitudes than they are at the surface. None of the  $\alpha$ -components consistently match the long-term variation common to all components of the magnetic field. For  $\alpha_{\phi\phi}^v$ , the northern and southern hemispheres exhibit quite distinct long-term trends, with reversals occurring out of phase and persisting for variable periods and intensity. Relating these to the variation in the magnetic cycles is not self-evident.

The long-term trends visible in  $\alpha_{ii}^v$  at both the base and the surface are not obviously correlated with the parity trends for the total field, depicted in the “barcode” on top of the data in Figure 4. The parities of all the diagonal components of the  $\alpha$ -tensor are very close to being purely antisymmetric at the surface at all times of the simulation, while much more significant deviations from pure antisymmetry occur at the base of CZ.

An interval of interest is the untypically strong cycle in  $\alpha_{\phi\phi}^v$  around 200 years in the northern hemisphere, which also coincides with the “missing cycle” in the surface magnetic field

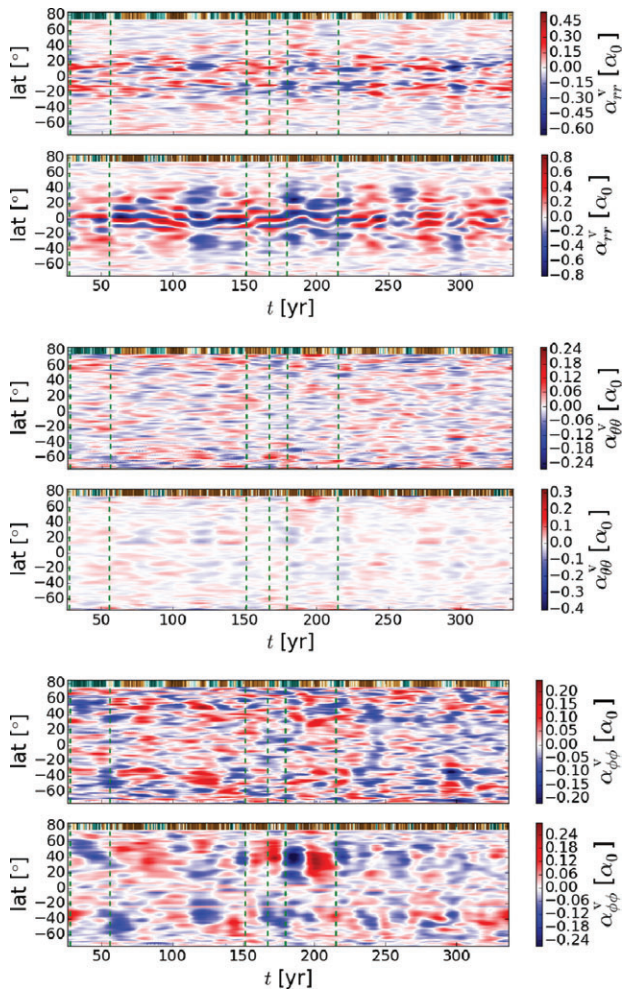


**FIGURE 4** Time–latitude plot of smoothed variation of the diagonal components of  $\alpha$ . Pairs of slices from the surface (upper) and base (lower) of the convection zone (CZ). The variations have been multiplied by the sign of the time average to identify enhancement (diminution) of the time-averaged tensor profile. The smoothing window is approximately 50 years. The parity of the total magnetic field across the slice is depicted by the “barcode” along the top (brown–green,  $-1$  to  $1$ ). Vertical lines (green, dashed) indicate three epochs examined in detail.

visible in Figure 1, panels 1 and 2. This epoch is identified by the last pair of vertical lines and is investigated in Section 3.2.3.

### 3.2.2 | Parity switching

We now consider two intervals during the evolution of the surface magnetic field when the parity of the total field remains either quadrupolar or dipolar for a longer period of time. The “quadrupole epoch” is 27–54 years, which has even parity at the surface, and the “dipole epoch” is 151–166 years. These are identified by the first two pairs of vertical green lines marked in Figures 1, 2, and 4. By contrasting the behavior of the transport coefficients during these epochs, we seek to identify how they act on the quadrupolar and dipolar modes of the dynamo.

In Figure 5, we show the time evolution of the parity during these epochs of each magnetic field component and the

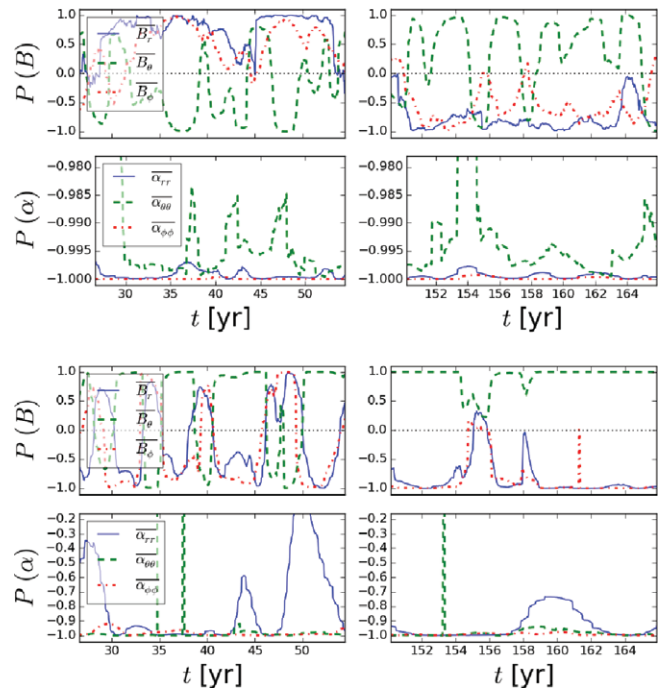


**FIGURE 5** Parity time series of magnetic field components and diagonal components of  $\alpha$  with 12.5-year smoothing window for surface (upper pair) and base (lower pair) of the convection zone (CZ). The left (right) column depicts the “quadrupole (dipole) epoch” defined by the total magnetic field parity near the surface. Note that for total field parity of  $\pm 1$ , the parity of  $B_\theta$  is  $\mp 1$ . The spikes, in particular, in the lowest panels are caused by values of  $\alpha$ -components being close to zero.

diagonal components of  $\alpha$ . As may reasonably be anticipated, the magnetic field components near the surface typically match parity with the total field (first row), although  $\bar{B}_\theta$  most commonly least matches the total field parity. During these intervals, the parity of the total field at the base does not necessarily align with that at the surface. Typically, the field parity at the base throughout the whole simulation is more consistently negative (dipolar) than that at the surface. During the “quadrupole epoch,” there are significantly more deviations from dipole at the base, than during the “dipole epoch,” although these need not be related. At the surface, the  $\alpha$ -components have strong negative parity during both dipole and quadrupole epochs, with a modest deviation most evident in  $\alpha_{\theta\theta}$ . Although still strongly negative, there are stronger deviations in the  $\alpha$ -components at the base, particularly in  $\alpha_{rr}$ , and this is more pronounced when the magnetic field has more quadrupolar composition. The  $\alpha_{rr}$ -variations are clearly in antiphase with those of the magnetic field, but it is difficult to establish whether the variations in the  $\alpha$ -components cause the changes in the field parity or vice versa. The variations of  $\alpha_{rr}$  at the base seem to be rather tightly anticorrelated with the surface  $\bar{B}_\theta$ . So  $\alpha_{rr}$  may affect parity at the base and seems to be connected with the  $\bar{B}_\theta$  parity evolution, but the parity variations of other  $\alpha$ -components seem not to be significant.

To examine how the transport coefficients may differ by location between the “quadrupole” and “dipole epochs,” we calculate the time-averaged meridional profiles for each

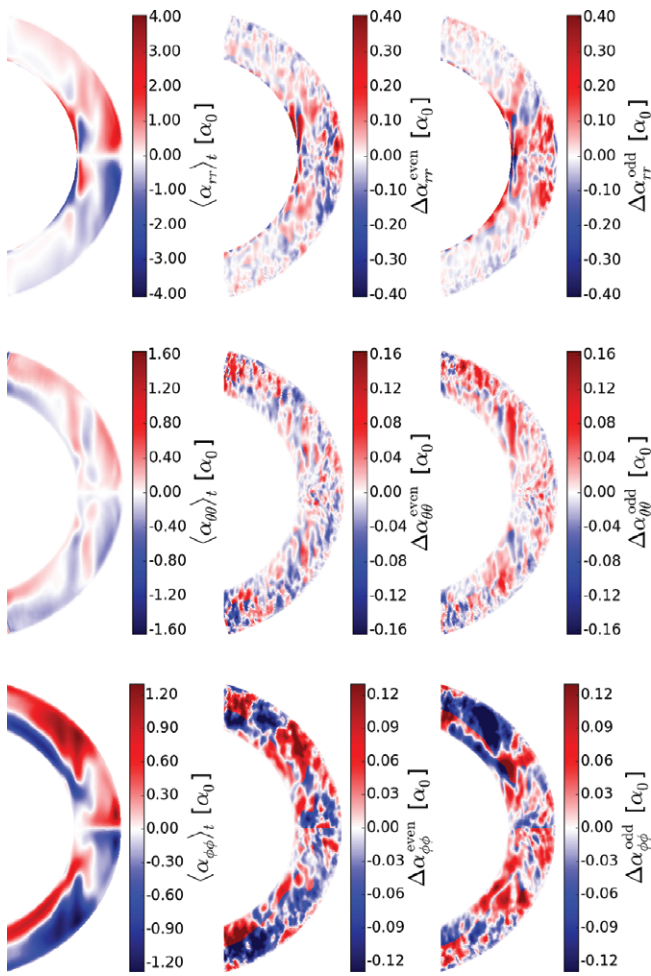


**FIGURE 6** Meridional plot left to right of  $\langle \alpha_{ii} \rangle_t$ , averaged over all time,  $\Delta\alpha_{ii}^{\text{even}}$ , averaged over the “quadrupole epoch” (27–54 years), and  $\Delta\alpha_{ii}^{\text{odd}}$ , averaged over the “dipole epoch” (151–166 years).  $\langle \alpha_{ii} \rangle_t$  is subtracted in the latter cases. The differences are multiplied by the sign of  $\langle \alpha_{ii} \rangle_t$ , to identify enhancement (diminution) relative to the total time average.

epoch and compare these to the time average for the whole simulation. In Figure 6, the diagonal components of  $\alpha$  are displayed as a time average across the total duration of the simulation  $\langle \alpha_{ii} \rangle_t$ . To visualize the difference between the two epochs and the time-averaged coefficients, we define

$$\begin{aligned}\Delta\alpha_{ii}^{\text{odd}} &= \langle \alpha_{ii} \rangle_{\text{odd}} - \langle \alpha_{ii} \rangle_t, \\ \Delta\alpha_{ii}^{\text{even}} &= \langle \alpha_{ii} \rangle_{\text{even}} - \langle \alpha_{ii} \rangle_t,\end{aligned}$$

where “even” references to the “quadrupole epoch” and “odd” to the “dipole epoch.” These are displayed in the latter two columns, multiplied by the sign of the simulation average, so that positive (negative)  $\Delta\alpha_{ii}$  indicates enhancement (diminution) of the tensor relative to its average.

$\alpha_{rr}$  is symmetrically enhanced near the equator during the “dipole epoch,” meaning that the  $\alpha$ -effect is amplified evenly in both hemispheres during this phase. The deviations from odd parity seen during this epoch, in the lowest right panel of Figure 5, are likely to be related to the narrow low-latitude region at the base of the CZ, where  $\alpha_{rr}$  is less symmetrically enhanced or quenched. It is less antisymmetric during the “quadrupole epoch,” caused by the less symmetric

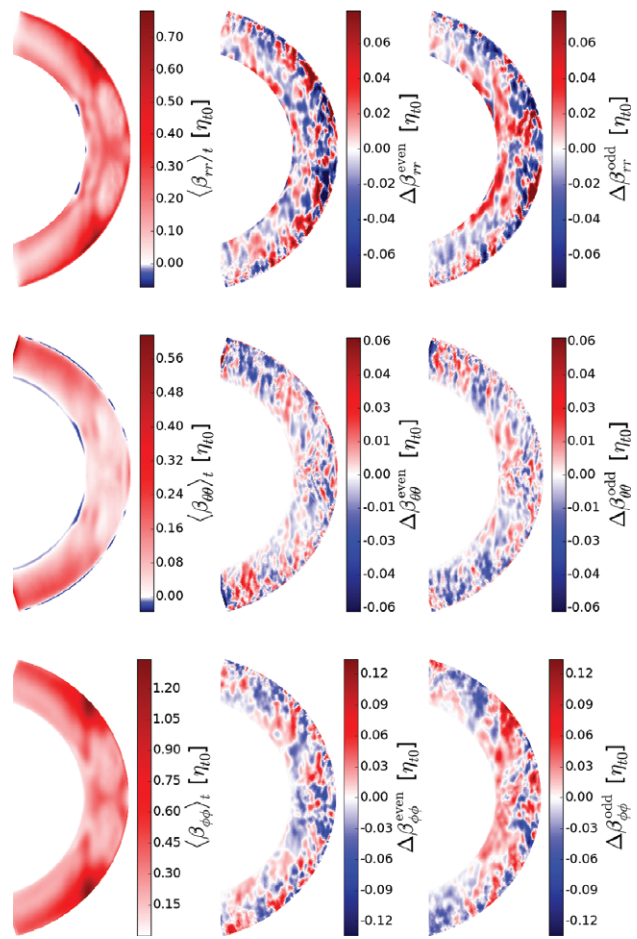


**FIGURE 7** The same as Figure 6, but for the diagonal  $\beta$ -components.

modification profile, and as a total, the coefficient is weakly reduced. While  $\alpha_{\theta\theta}$  does not seem to be significantly modified comparing these two states,  $\alpha_{\phi\phi}$  shows a similar pattern as  $\alpha_{rr}$ : During the “dipole epoch,” the quantity is symmetrically modified, while during the “quadrupole epoch,” the modification is more antisymmetric. This results in a tendency of the coefficient to remain close to antisymmetry during a dipole phase, while some deviations from pure antisymmetry are seen during the quadrupole phase. These deviations, however, are smaller for  $\alpha_{\phi\phi}$  than for  $\alpha_{rr}$ , which can also be seen from Figure 5. Although there are very strong local regions of enhancement and reduction of  $\alpha_{\phi\phi}$ , the net effect remains small.

The same calculations are illustrated in Figure 7 for the turbulent diffusion tensor  $\beta$ , which, when averaged over whole time, are typically positive and symmetric about the equator. Very small negative regions appear close to the equator at the base for  $\beta_{rr}$  and  $\beta_{\theta\theta}$  and for the latter also in a narrow layer near the surface. In Warnecke et al. (2017), the authors also performed a detailed study, using all the  $\beta$ -tensor coefficients, on the possibility for negative magnetic diffusion, leading to dynamo action instead of diffusive effects, but concluded that such effects are probably negligibly small in a similar system as studied here. Similar to the  $\alpha$ -components, the  $\beta$ -components are more

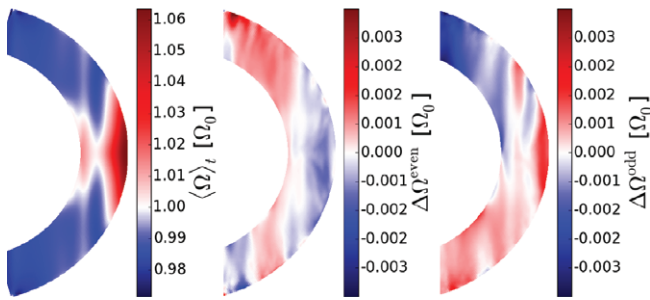


FIGURE 8 The same as Figure 6, but for  $\Omega$ .

symmetrically enhanced/reduced during the odd phase, while the modification is more antisymmetric during the even phase. The overall reduction/enhancement, however, is rather small. Although referring to much simpler systems than considered here, Rädler (1986) identified mean-field solutions, in which lower dynamo numbers (high  $\beta$ ) tend to excite dipolar fields, while higher dynamo numbers (low  $\beta$ ) quadrupolar.

It is also informative to compare how the differential rotation profile  $\Omega = \bar{U}_\phi[r \sin\theta]^{-1} + \Omega_0$  adjusts during the two different epochs and we define  $\Delta\Omega^{\text{odd/eve}} = \langle\Omega\rangle_{\text{odd/eve}} - \langle\Omega\rangle_t$ . In Figure 8, the change in  $\Omega$  during each epoch indicates that during the “quadrupole epoch,” the surface near the equator slows down and the tangent cylinder speeds up. During the “dipole epoch,” the equatorial surface speeds up, and the north (south) pole speeds up (slows down). The tangent cylinder also slows. Note that the asymmetry evident in  $\Delta\Omega$  during the “dipole epoch” would not arise due to the antisymmetric magnetic field, as the Lorentz force is quadratic in  $B$ . There must be a transient N-S gradient in magnetic energy associated with this epoch. From Figure 5, we observe that this is not a pure dipole, so such gradients can be present. Most importantly, the region of negative shear in the midlatitudes, which has been found to be instrumental in producing the equatorward propagation of the dynamo wave, is reduced (enhanced) during the “quadrupole (dipole) epochs.” This may be the cause of the tendency to observe less regular migration pattern and disrupted cycles during the quadrupolar states. The differences, however, are less than 1%, compared to an overall spread in the time-averaged differential rotation rate of 10%, and the verification of this hypothesis will have to wait for a dedicated mean-field investigation of the system.

### 3.2.3 | Missing cycle

In Section 3.2.1, we identify an interval, during which a strong variation in  $\alpha_{\phi\phi}$  at the base of the CZ coincides with the missing cycle at the surface. In Figure 9, we plot the parity of the magnetic field and diagonal components of  $\alpha$  during this epoch 175–215 years near the surface and the base. During the “missing cycle” epoch, the surface field moves from the predominantly symmetric state to an antisymmetric one. This means that the parity of the surface field changes from 1 to  $-1$  during a roughly 10-year time interval. During the “missing cycle,” the base field is highly antisymmetric, and

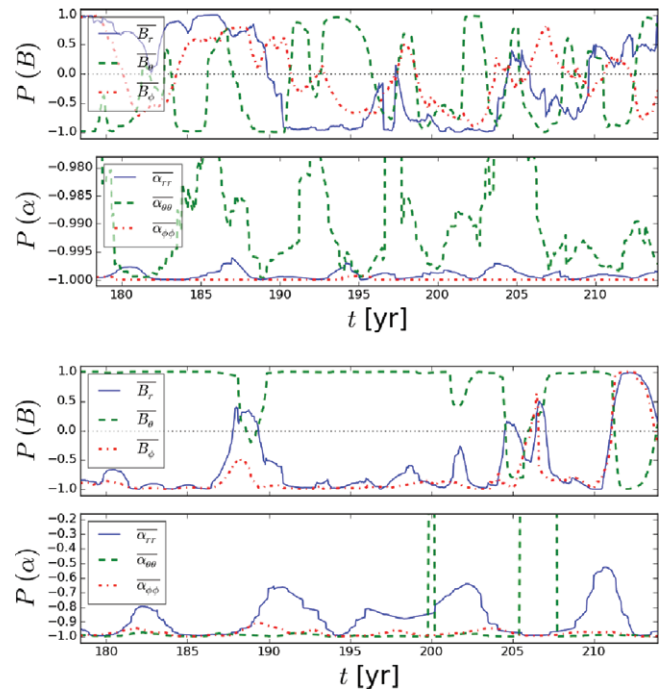
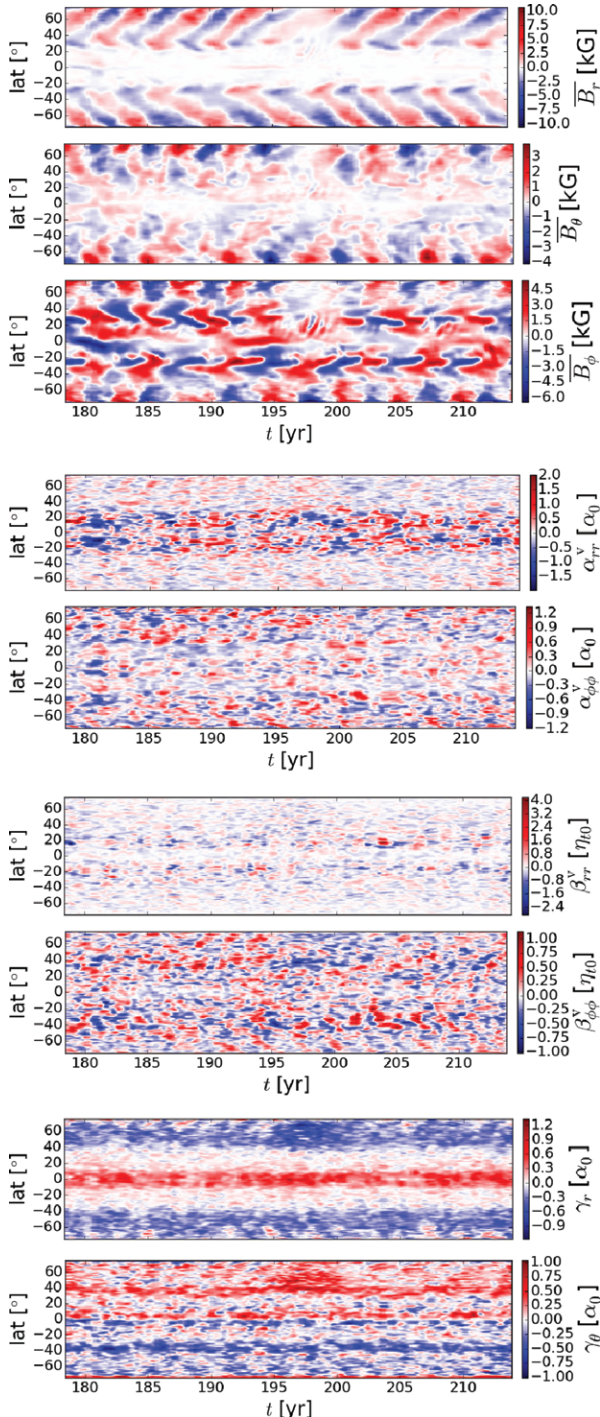


FIGURE 9 Parity time series of the magnetic field components and diagonal components of  $\alpha$  with 12.5-year smoothing window for surface (upper pair) and base (lower pair) of the convection zone (CZ). Note that for total field parity of  $\pm 1$ , the parity of  $B_\theta$  is  $\mp 1$ . The time segment corresponds to an epoch of disruption in the surface magnetic field, including a “missing cycle” in the northern hemisphere, and strong  $\alpha_{\phi\phi}$ -component near the base.

after surface activity is re-established, the surface field parity starts again rapidly migrating toward 1. Such rapid changes in the magnetic field parity are very common throughout the simulation, but no other such epoch is observed to produce significantly reduced cycles. In addition, the “missing cycle” epoch is not preceded or followed by any peculiar behavior in the parities of the diagonal  $\alpha$ -coefficient. This hints toward the parity evolution being unimportant as a cause of the missed cycle.

Explanation for this behavior must, therefore, be sought elsewhere. For a closer inspection of the dynamics around the “missing cycle” in Figures 10, 11, and 12, we zoom into the epoch 175–215 years. In Figure 10, we display the surface magnetic field components and some of the more interesting transport coefficients at the surface. From the first three panels, we can see that during the “missing cycle,” between 197 and 202 years, the strength of all  $\bar{B}$  components is reduced, particularly those of  $\bar{B}_r$  and  $\bar{B}_\phi$ . In addition, there is an enhanced high-frequency variability around  $20^\circ\text{N}$  with a cycle length less than 1 year, most pronounced in  $\bar{B}_\phi$ . Such a short cycle is normally always present as the third, rather incoherent and poleward dynamo cycle (see the analysis in Käpylä et al. 2016; Olspt et al. 2016), and it was observed to persist even during the grand minimum-type event seen in Käpylä et al. (2016), consistent with the findings here. Warnecke et al. (2017) found indication that this short cycle can be caused by a locally operating  $\alpha^2$  dynamo near the surface. Coincident with the surface field suppression, the field at the



**FIGURE 10** Zoom-in of “missing cycle” (175–215 years), time–latitude plots of the magnetic field components and selected turbulent transport coefficients, with 2.5-year smoothing window near the surface. For  $\alpha_{ii}^v$  and  $\beta_{ii}^v$ , time averages are subtracted and the result is multiplied by the sign of the time averages. For  $\gamma_i$ , no time average is subtracted.

base of the CZ obtains a local maximum in particular in  $\bar{B}_r$  and  $\bar{B}_\theta$ , as shown in the two top panels of Figure 11. Very similar behavior was observed by Käpylä et al. (2016) during a more extended suppression of the surface activity, when also the enhancement of the base magnetic field was stronger than in the current simulation.

The surface  $\alpha$ -tensor components show no particularly interesting behavior before the “missing cycle,” but are clearly

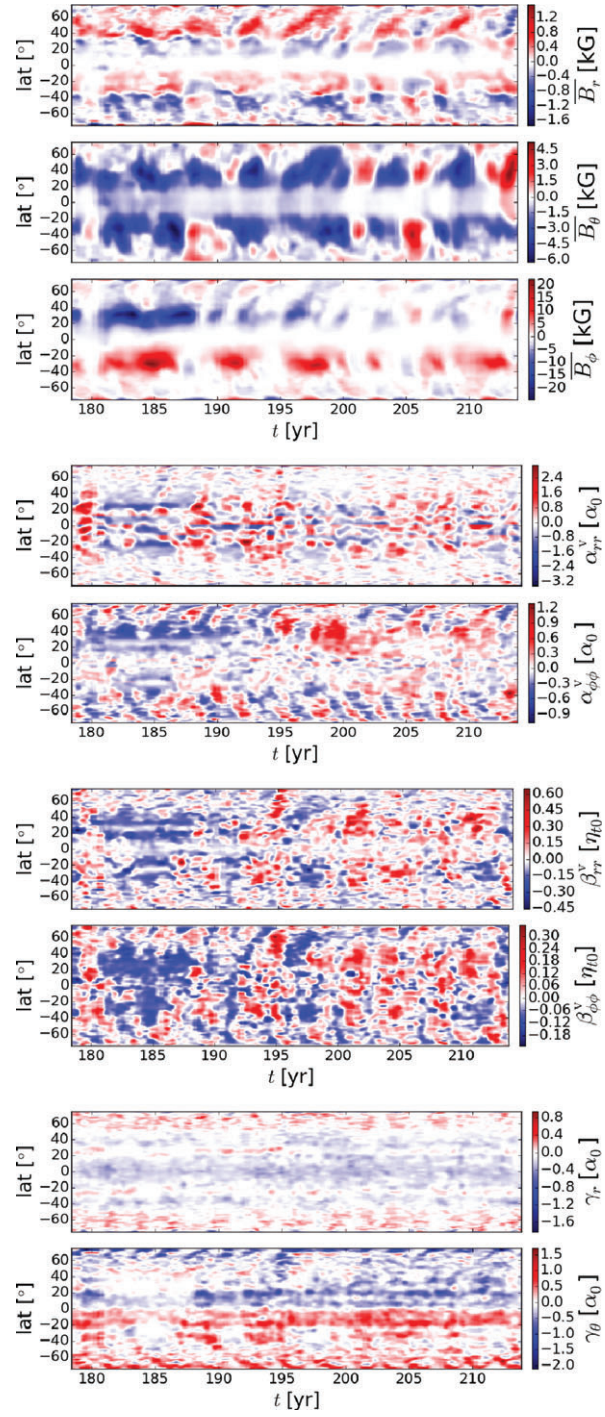


**FIGURE 11** Zoom-in of “missing cycle” (175–215 years), time–latitude plot of the magnetic field components and selected turbulent transport coefficients, with 2.5-year smoothing window near the base of the convection zone. For  $\alpha_{ii}^v$  and  $\beta_{ii}^v$ , time averages are subtracted and the result is multiplied by the sign of the time averages. For  $\gamma_i$ , no time average is subtracted.

reduced during it.  $\beta_{rr}$  at the surface is somewhat enhanced before the event and reduced after it, but this variation is rather small. The corresponding coefficients at the bottom, however, show more interesting trends, which become better visible when smoothing is applied (see Figure 4). Especially,  $\alpha_{\phi\phi}$  becomes strongly reduced in the north for several years before the event and is enhanced after it. A similar tendency, however, is seen also in the  $\beta$ -tensor, and therefore, the

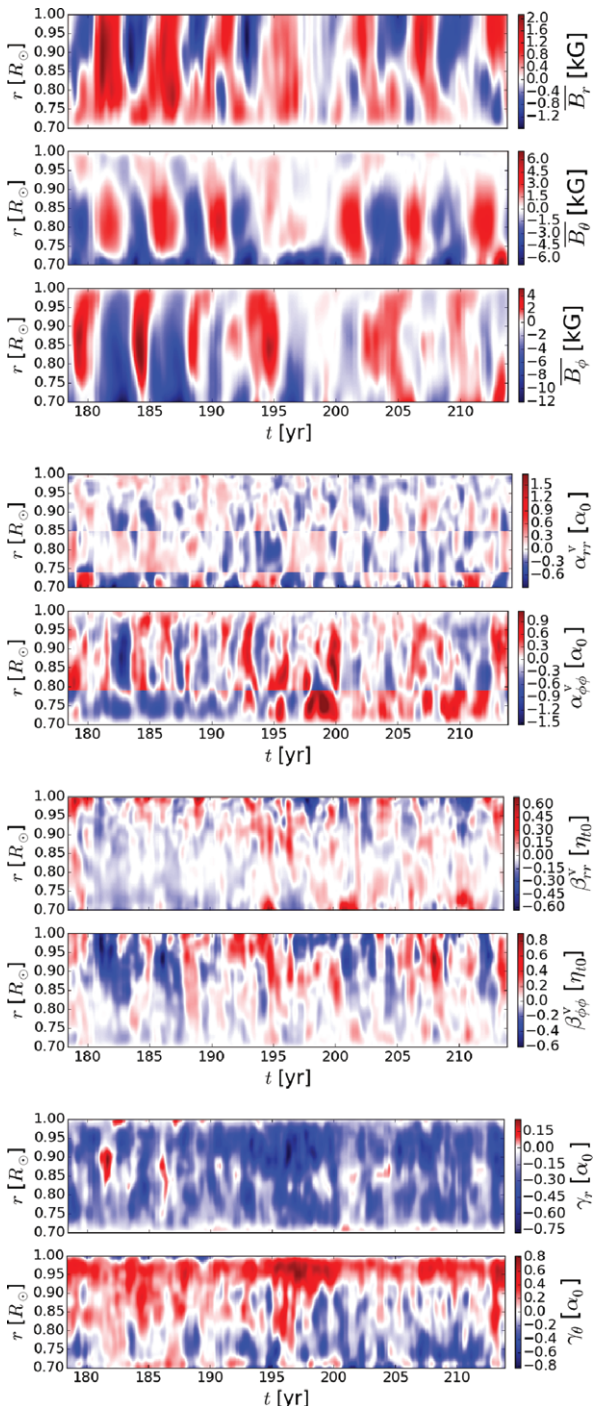


**FIGURE 12** Zoom-in of “missing cycle” (175–215 years), time–radius plot of the magnetic field components and selected turbulent transport coefficients, with 2.5-year smoothing window at a fixed latitude. For  $\alpha_{rr}^v$  and  $\beta_{rr}^v$ , time averages are subtracted and the result is multiplied by the sign of the time averages. For  $\gamma_i$ , no time average is subtracted. The mean of 10 latitudes straddling  $40.6^\circ\text{N}$  is used for the radial profile.

strong reduction of  $\alpha_{\phi\phi}$  appears to be compensated by the simultaneous reduction of the diffusivities. Therefore, it is not obvious that any great impact on the dynamo efficiency would be expected, but this should be confirmed from a mean-field analysis.

Perhaps, the most interesting behaviour is seen in the turbulent pumping  $\gamma$ : During the “missing cycle,” the radial component  $\gamma_r$ , directed mostly downward at high latitudes,

is strongly enhanced. This means that the magnetic field is more efficiently pumped downward during this epoch. At the same time, similar enhancement in the latitudinal turbulent pumping  $\gamma_\theta$  is seen at a corresponding location in latitude. As the latitudinal pumping here is directed toward the equator, this means that the magnetic field was transported more efficiently toward low latitudes during the “missing cycle”. The enhancement of the magnetic field in the bottom of the CZ is likely to be due to the enhancement seen in the turbulent pumping.

In order to verify our conclusions based on the inspection of time–latitude plots, we finally inspect some time–radius plots. We take a latitudinal mean over 10 grid points, straddling the approximate locus of the “missing cycle” event at  $40.6^\circ\text{N}$ . Figure 12 contains the time–radius profiles of this slice for the magnetic field components and selected turbulent transport coefficients. This reveals that the region of reduced magnetic field strength permeates deep within the CZ, evolving earliest at the surface in  $\bar{B}_\theta$  before 195 years, a clear reduction in the magnetic field strength occurring even earlier than that in the mid-depths for  $\bar{B}_\theta$ .

With respect to the turbulent transport, the reduction of  $\alpha_{\phi\phi}$ ,  $\beta_{rr}$ , and  $\beta_{\phi\phi}$  prior to the event itself, also detectable in the time–latitude slices, is more clearly seen in the time–radius plots. The latter, however, better illustrate how these effects are differently distributed in depth. The reduction of  $\alpha_{\phi\phi}$  occurs only in a narrow layer at the base of CZ, while  $\beta_{rr}$  is reduced almost at every depth except at the surface and  $\beta_{\phi\phi}$  is reduced strongest at the topmost half of the CZ. Therefore, the implications for the dynamo efficiency are not so straightforward as implied by the time–latitude slices.

#### 4 | CONCLUSIONS

In this paper, we have presented the first results of an analysis that measures the turbulent transport coefficients in a solarlike convective dynamo solution with irregular long-term behavior. We have particularly focused on two special properties seen in the dynamo solution, namely the erratic-looking parity switches (competition between dipolar and quadrupolar dynamo modes) and the abrupt disappearance and re-emergence of surface magnetic activity.

Our analysis revealed that the parity switches may be linked to variations seen in the parity of the turbulent transport coefficients themselves, especially related to the  $\alpha_{rr}$ -component near the bottom of the CZ. We also found an indication that during a “quadrupole epoch,” the region of negative shear in the midlatitudes, a prominent feature present in many convection simulations and shown to be responsible for the equatorward migration (Warnecke et al. 2014), becomes suppressed, and this may lead to more chaotic-appearing migration patterns.

During the “missing cycle,” we observed a disappearance of surface magnetic activity lasting roughly one magnetic

cycle of five years in the northern hemisphere. Simultaneously, we observed intensification of the magnetic field at the base of the CZ. Although this epoch does not really represent a grand minimum, this behavior is very similar to that found by Käpylä et al. (2016) from their simulation exhibiting a more extended minimum epoch. Our test-field analysis provides a plausible explanation in terms of the reduction of  $\alpha_{\phi\phi}$  prior to the reduced surface activity and enhanced turbulent downward pumping during the event, confining some of the magnetic field at the bottom of the CZ. At the same time, however, a quenching of the turbulent magnetic diffusivities is observed, albeit distributed somewhat differently by depth compared to the  $\alpha$ -components. Hence, to determine the effect of these modifications to the turbulent transport coefficients on the dynamo efficiency, dedicated mean-field modeling is required.

## ACKNOWLEDGEMENTS

We gratefully acknowledge the input of Axel Brandenburg, Petri J. Käpylä, and Matthias Rheinhardt to this work. The financial support from the Academy of Finland (ReSoLVE Centre of Excellence, grant no. 272157; F.A.G., M.J.K.) is acknowledged. J.W. acknowledges funding from the People Programme (Marie Curie Actions) of the European Union's Seventh Framework Programme (FP7/2007-2013) under REA grant agreement no. 623609. The simulations were performed using the supercomputers hosted by the CSC—IT Center for Science Ltd. in Espoo, Finland, which is administered by the Finnish Ministry of Education.

## REFERENCES

- Augustson, K., Brun, A. S., Miesch, M., & Toomre, J. 2015, *ApJ*, 809, 149.  
 Beaudoin, P., Simard, C., Cossette, J.-F., & Charbonneau, P. 2016, *ApJ*, 826, 138.

- Brandenburg, A., Chatterjee, P., Del Sordo, F., et al. 2010, *Phys. Scripta*, 142, 014028.  
 Ghizaru, M., Charbonneau, P., & Smolarkiewicz, P. K. 2010, *ApJ*, 715, L133.  
 Guerrero, G., Smolarkiewicz, P. K., de Gouveia Dal Pino, E. M., et al. 2016, *ApJ*, 819, 104.  
 Käpylä, P. J., Mantere, M. J., & Brandenburg, A. 2012, *ApJ*, 755, L22.  
 Käpylä, P. J., Mantere, M. J., Cole, E., et al. 2013, *ApJ*, 778, 41.  
 Käpylä, P. J., Käpylä, M. J., & Brandenburg, A. 2014, *A&A*, 570, A43.  
 Käpylä, M. J., Käpylä, P. J., Olspt, N., et al. 2016, *A&A*, 589, A56.  
 Käpylä, P. J., Käpylä, M. J., Olspt, N., et al. 2017, *A&A*, 599, A5.  
 Krause, F., & Rädler, K.-H. 1980, *Mean-field Magnetohydrodynamics and Dynamo Theory*, Pergamon Press (Oxford).  
 Norton, A. A., Charbonneau, P., & Passos, D. 2014, *Space Sci. Rev.*, 186, 251.  
 Olspt, N., Kapyla, M. J., & Pelt, J. 2016, *2016 IEEE International Conference on Big Data, BigData 2016*, IEEE XPLOR Digital, Washington DC, USA, December 5–8, 3214–3223.  
 Ossendrijver, M., Stix, M., Brandenburg, A., & Rüdiger, G. 2002, *A&A*, 394, 735.  
 Parker, E. N. 1955, *ApJ*, 122, 293.  
 Passos, D., & Charbonneau, P. 2014, *A&A*, 568, A113.  
 Racine, É., Charbonneau, P., Ghizaru, M., et al. 2011, *ApJ*, 735, 46.  
 Rädler, K.-H. 1969, *Veröffentl. Geod. Geophys.*, 13, 131.  
 Rädler, K.-H. 1986, *Astron. Nachr.*, 307, 89.  
 Schrinner, M., Rädler, K.-H., Schmitt, D., et al. 2005, *Astron. Nachr.*, 326, 245.  
 Schrinner, M., Rädler, K.-H., Schmitt, D., et al. 2007, *Geophysical and Astrophysical Fluid Dynamics*, 101, 81.  
 Schrinner, M., Petitdemange, L., & Dormy, E. 2012, *ApJ*, 752, 121.  
 Steenbeck, M., Krause, F., & Rädler, K.-H. 1966, *Zeitschrift Naturforschung Teil A*, 21, 369.  
 Warnecke, J., Käpylä, P. J., Käpylä, M. J., & Brandenburg, A. 2014, *ApJ*, 796, L12.  
 Warnecke, J., Käpylä, P. J., Käpylä, M. J., & Brandenburg, A. 2016, *A&A*, 596, A115.  
 Warnecke, J., Rheinhardt, M., Tuomisto, S., et al. 2017, *A&A*, in press, arXiv:1601.03730.  
 Yoshimura, H. 1975, *ApJ*, 201, 740.

**How to cite this article:** Gent FA, Käpylä MJ, Warnecke J. Long-term variations of turbulent transport coefficients in a solarlike convective dynamo simulation, *Astron. Nachr. / AN*. 2017;338:885–895. <https://doi.org/10.1002/asna.201713406>.